Analyst

ROYAL SOCIETY OF CHEMISTRY

PAPER

View Article Online
View Journal | View Issue

Open Access Article. Published on 16 January 2023. Downloaded on 3/24/2023 9:50:45 AM.
This article is licensed under a Creative Commons Attribution 3.0 Unported Licence.

Check for updates

Cite this: *Analyst*, 2023, **148**, 1123

# Conical shell illumination incorporating a moving aperture for depth-resolved high-energy X-ray diffraction

Daniel Spence,[a] Anthony Dicken,[a] David Downes,[a] Keith Rogers[b] and Paul Evans *[a]

Received 9th November 2022,
Accepted 14th January 2023

DOI: 10.1039/d2an01842j

rsc.li/analyst

In many applications, the main limitation of X-ray absorption methods is that the signals measured are a function of the attenuation coefficient, which tells us almost nothing about the chemical or crystallographic nature of objects under inspection. To calculate fundamental crystallographic parameters requires the measurement of diffracted photons from a sample. Standard laboratory diffraction methods have been refined for well over a century and provide 'gold standard' structural models for well-prepared samples and single crystals but have little applicability for thick heterogeneous samples as demanded by many screening applications. We present a new high-energy X-ray diffraction probe, which in comparison with previous depth-resolving hollow beam techniques, requires a single beam, point detector and a simple swept aperture to resolve sample signatures at unknown locations within an inspection space. We perform Monte Carlo simulations to support experiments on both single- and multiple-material localisation and identification. The new probe is configured and tested using low-cost commercial components to provide a rapid and cost-effective solution for applications including explosives detection, process control and diagnostics.

## Introduction

X-ray diffraction (XRD) techniques for probing molecular structures within heterogeneous objects can be greatly beneficial to fields including explosives detection systems,[1–3] food quality and safety,[4] combinatorial screening,[5] bone quality,[6–8] and cancer diagnostics.[9] The versatility of X-rays as a non-destructive 'molecular' probe stems from their relatively short wavelength of the order of $10^{-10}$ m.[10] Probing photons can interact with the sample's molecular structure to produce coherently scattered (signal) photons, which can escape from the sample without energy loss. The knowledge of both the energy and trajectory of such photons enables the calculation of material characterisation information. This process is the basis of crystallography and powder diffraction.[11] However, while X-ray diffraction (XRD) offers perhaps the most specific method of material phase identification it remains restricted to the laboratory. For example, although some microbeam systems are air-cooled, most standard laboratory diffractometers usually require water cooling as thermionic X-ray generation is <1% efficient. However, the relatively low energy of the interrogating photons *e.g.*, Cu Kα radiation ~8 keV results in near-surface specimen depths of around a fraction of a mm. Thus, while the standard method has been refined for well over a century and provides 'gold standard' structural resolution for well-prepared samples and single crystals it has little applicability for thick heterogeneous samples. The evaluation of extended regions of interest along the probing direction requires at least an order of magnitude increase in photon energies for many screening applications. For example, the detection of concealed explosives in aviation luggage screening usually requires ~140 keV photons. In addition, a practical probe would require resolving explosives at unknown positions along the beam in the presence of 'cluttering' materials both of which individually would confound a standard approach.

Recent developments in XRD-based, spatially resolved materials identification techniques often require collimation into narrow pencil, or fan beams and can require either extended measurement times,[12] or powerful X-ray sources,[13] to ensure sufficient photon statistics for material identification. Rapid material identification by energy-dispersive XRD is possible at 48 mAs to 0.4 mAs but at the expense of spatial resolution.[14] In addition, tomographic XRD implementation strategies have been investigated including 3DXRD,[15] TEDDI,[16,17] XDi,[18] SICSI,[13] and XRD-CT,[19–23] and all have been individually adapted to their proposed applications.

[a]*Imaging Science Group, Rosalind Franklin Building, Clifton, Nottingham Trent University, Nottingham, UK. E-mail: paul.evans@ntu.ac.uk*
[b]*Cranfield Forensic Institute, Cranfield University, Shrivenham, Swindon, UK*

Open Access Article. Published on 16 January 2023. Downloaded on 3/24/2023 9:50:45 AM.
This article is licensed under a Creative Commons Attribution 3.0 Unported Licence.

Focal construct technology (FCT) is a technique, which uses an annular beam of radiation and has been designed to improve such shortcomings.[24–26] When an annular beam is incident normally on a semi- or polycrystalline material, Debye cones with well-understood energy and angular relationships[11] are produced from each point of intersection within an annular gauge volume. These Debye cones overlap downstream in the imaging chain resulting in significantly increased scattered signal intensity.[24] FCT has been shown to deal favourably with non-ideal samples such as those exhibiting large grain size, preferred orientation (or texture),[27] and liquid samples,[28] that only exhibit short-range order. New incarnations of the FCT technique designed to work in an energy-dispersive mode (ED-FCT),[27,29] using a polychromatic X-ray beam and energy-resolving point detector exhibit advantages over angular-dispersive FCT (AD-FCT),[30–32] in terms of measurement time reduction, although with some trade-off against *d*-spacing resolution. In summary, prior FCT methods without collimation or modulation of the diffraction signal require the position of the sample in the beam is known to calculate structural parameters such as *d*-spacings. Although, AD-FCT tomography overcomes this limitation it requires raster scanning a sample through the beam and a spatially resolving detector to measure the diffracted flux.[33]

Depth-resolved ED-FCT has recently been developed by using a two-dimensional pixelated energy-resolving detector, receiving scattered flux from the sample *via* a ~2 mm pinhole between the sample and detector. The pinhole acts as a $2\theta$ selector to provide information about the spatial origin of coherently scattered photons incident on the detector.[34] Alternatively, an energy-resolving point detector can replace the pinhole. In which case, to determine $2\theta$, the sample must be scanned through a dual configuration of shell beams,[35] each configured with a central detector. To recap, the former approach requires an expensive pixelated detection surface, while the latter requires 2× point detectors together with dual beam optics and a sample scanning mechanism.

Here we investigate a novel X-ray diffraction system, which combines the advantages of both the 'pinhole' and 'dual beam' ED-FCT approaches by combining a single interrogating beam and point detector *i.e.*, without the requirement for pixelated detectors or dual beams/optics and sample translation. Instead, objects under inspection are illuminated with a similar polychromatic annular X-ray beam but with a much wider circular XRD collection aperture, ~10 mm diameter optically coupled to an energy-resolving single-pixel detector. Depth information is recovered by translating the aperture along the symmetry axis of the system, providing a cumulative interrogation of a three-dimensional object, along one axis ($z$).

We perform Monte Carlo simulations to support experiments on both single- and multiple-material localisation and identification.[36]

The method described in this work uses commercial, off-the-shelf, low-cost components and has the potential to significantly enhance performance in areas such as security and industrial process control where cost-effective solutions are an important factor.

# Experimental section

## Materials

In this work we attempt to identify signature diffraction patterns of sucrose ($C_{12}H_{22}O_{11}$), calcite ($CaCO_3$) and calcium hydroxide ($Ca(OH)_2$). All materials are crystalline powders contained within sealed plastic cylindrical containers, with diameter, $2R_s$ = 90 mm and depth, $t$ = 15 mm.

## Instrumentation

We perform experiments and simulations, which are analogous to our swept-aperture concept, see Fig. 1, by implementing discrete increments of the aperture position along the $z$-axis.

A polychromatic Hamamatsu point X-ray source, operating at 130 kV, 300 μA illuminates a bespoke tungsten optic, which transmits a conical shell of primary X-rays with a mean half-opening angle $\phi_{avg}$ = 3.92° and beam divergence $\Delta\phi$ = 0.05°, as described in detail elsewhere.[27] At some distance downstream of the X-ray source is an Amptek XR-100T-CdTe energy-resolving detector module with a 3 mm diameter detection surface. The detector is placed at $z_d$ = 690 mm at the origin of the $x - y$ plane. Energy resolution of the detector is ~850 eV with a total energy range of 1–130 keV.

Where the primary X-ray cone intersects a material with long-range order, placed between the X-ray source and detector, photons are diffracted under the satisfaction of Bragg's condition. The diffraction angle for a subset of these photons enables them to be received on the detector at $z_d$ and are measured by photon counting.

A circular aperture of radius, $r_a$ = 4.5 mm, rests initially in a position between the X-ray source and the detector, downstream of the inspection region of interest. The aperture transmits only scattered photons generated at the intersection of the primary X-ray cone from a potential conical volume element in space defined by the lines-of-sight of the extrema of the two-dimensional detector, through the aperture, see Fig. 2. As the aperture is translated along the $z$-axis, towards the detector, the specimen volume increases for relatively thick samples. For example, at some point a cumulative scatter

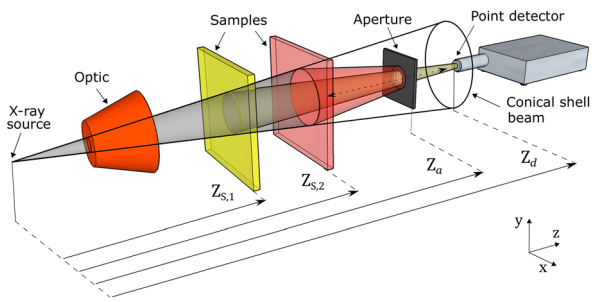


**Fig. 1** Concept image of the swept aperture system with crystalline samples at $z$-axis positions, $z_{s,1}$ and $z_{s,2}$; circular aperture at $z_a$ and energy-resolving detector at $z_d$. The aperture selects upper limits in $z$-space observed by the detector.

 This journal is © The Royal Society of Chemistry 2023

Open Access Article. Published on 16 January 2023. Downloaded on 3/24/2023 9:50:45 AM.
This article is licensed under a Creative Commons Attribution 3.0 Unported Licence.

signal is received at the detector from the entire intersection volume for $z \leq z_{max}$, as determined by the aperture dimensions and relative position during the translation.

Depth information is recovered by evaluating the additional photons transmitted through the aperture (and reaching the detector) with each increment in its position, $z_a$ relative to the previous position, $z_a - \Delta z_a$ where$\Delta z_a$ is small. This is analogous to a continuously moving aperture where $\Delta z_a = z_a \Delta t$, and $z_a$ is the translation velocity of the aperture along the $z$-axis. With each new aperture position, the detector observes an additional contribution to the total diffraction signal, which can be assigned to some additional specimen/intersection region in space.

Considering the two-dimensional $y - z$ plane of the system represented in Fig. 1 (at $x = 0$), there are multiple intersection points ($Z_L$, $Z_B$, $Z_T$, $Z_R$) between the cone of primary X-rays and lines-of-sight of the extrema of the detector. The detector lines-of-sight are limited by the aperture dimensions and position, illustrated in Fig. 2.

For a given aperture increment, $z_a \rightarrow z_a + \Delta z_a$ the detector receives additional diffracted photons originating within the additional intersection of the "two volumes". There exists some central position, $z_C$ which the detector can be said to observe for a given aperture window $z_a \rightarrow z_a + \Delta z_a$. The locations of these intersection points are:

$$Z_T = \frac{r_d z_a + r_a z_d}{[r_d + r_a + (z_d - z_a)\tan(\phi_{max})]} \tag{1a}$$

$$Z_B = \frac{r_d z_a - r_a z_d}{[r_d - r_a + (z_a - z_d)\tan(\phi_{max})]} \tag{1b}$$

$$Z_R = \frac{r_d z_a + r_a z_d}{[r_d + r_a + (z_d - z_a)\tan(\phi_{min})]} \tag{1c}$$

$$Z_L = \frac{r_d z_a - r_a z_d}{[r_d + r_a + (z_a + z_d)\tan(\phi_{min})]}. \tag{1d}$$

We find that $\frac{Z_R - Z_T}{Z_R - Z_L} \ll 1$, which indicates that beam divergence is negligible in this system when considering the range of $z$-space observed by the detector for a given aperture position. The central position of the observation range can be assumed to be the mid-point between $Z_R$ and $Z_L$

$$z_C = \frac{1}{2}(Z_R + Z_L). \tag{2}$$

The aperture radius, $r_a$ and the detector half-width, $r_d$ are both fixed, as is the down-stream detector location $z_d$. The uncertainty in sample position is:

$$\Delta z_C = \frac{1}{2}(Z_R - Z_L). \tag{3}$$

Within the range of $Z_C$ observable in the above geometry, the presence of materials with long-range order will generate coherent scattering (diffraction) in the form of overlapping polychromatic Debye cones,[27] impinging on the detector. If the one-dimensional spatial density (along the $z$-axis) of each diffracting object is described by a Gaussian profile, the total diffracted photon count observed at the detector can be modelled as a linear sum of the integrals of these Gaussian profiles; each term in the sum corresponding to an individual sample, $S_n$ at position $z_{s,n}$. This *Linear Sum of Gaussian Integrals* (LSGI) model uses, as the integral of a Gaussian function, the *error function*. A constant term $c_{s,0}$ is included to account for system noise and miscellaneous scattering from the system upstream of the minimum interrogation volume.

$$f(z_C) = c_{s,0} + \sum_{n=1}^{N} \int_0^{z_j} A_n e^{-\left(\frac{z_C - z_{s,n}}{\sqrt{2}\sigma}\right)^2} dz_C \tag{4a}$$

$$f(z_C) = c_{s,0} + \sum_{n=1}^{N} a_n erf\left(\frac{z_C - z_{s,n}}{b}\right) \tag{4b}$$

The LSGI model's primary parameters are the set of $z_{s,n}$ indicating the presence of diffracted photons from the $n$th object entering the line-of-sight of the detector. To extract the contributing Gaussian profiles observed during the aperture sweep, we take the first derivative the LSGI fit.

$$f'(z_C) = \sum_{n=1}^{N} A_n e^{-\left(\frac{z_C - z_{s,n}}{\sqrt{2}\sigma}\right)^2} \tag{5}$$

The centres of the contributory Gaussians are identified by zero-crossing points in the second derivative of the LSGI fit. Having obtained estimates for the location of each diffracting material in $z$-space, one can calculate the appropriate $2\theta_n$ and material $d$-spacing values for corresponding photons arriving at the centre of the energy-resolving detector.

$$2\theta_n = \tan^{-1}\left(\frac{z_{s,n}\tan\phi_{avg}}{(z_d - z_{s,n})}\right) + \phi_{avg} \tag{6a}$$

And from Bragg's condition.

$$d_{\lambda,n} = \frac{\lambda}{2\sin\theta_n} \tag{6b}$$

Here, $2\theta_n$ is the diffraction angle; $\phi_{avg}$ is the average half-opening angle of the primary beam; $\lambda = \frac{hc}{E}$ is the wavelength

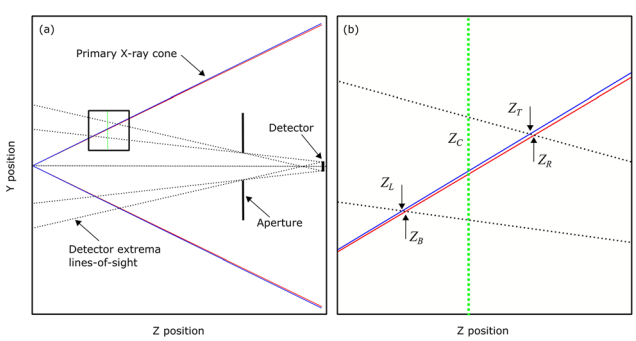


**Fig. 2** Two-dimensional side-view schematic of the swept aperture system with (a) intersection of the primary X-ray cone with lines-of-sight of detector and (b) close view of intersection points ($Z_L$, $Z_B$, $Z_T$, $Z_R$) and mid-point of detector observation range for a given aperture position ($z_C$).

Open Access Article. Published on 16 January 2023. Downloaded on 3/24/2023 9:50:45 AM.
This article is licensed under a Creative Commons Attribution 3.0 Unported Licence.

of diffracted photons observed at energy $E$; $h$ is Planck's constant and $c$ is the speed of light in a vacuum.

### Monte Carlo simulations

To support the experimental work, we simulate the response of an energy-resolved X-ray detector under similar-geometry, swept-aperture conditions to those described in previous sections.

Two systems are investigated; (i) a single sample with depth, $t$ = 15 mm comprised of sucrose ($C_{12}H_{22}O_{11}$), located at 220 mm from the X-ray source, and (ii) a series of two $t$ = 15 mm samples, calcium hydroxide ($Ca(OH)_2$) and calcite ($CaCO_3$), the former being positioned at 160 mm from the source and the latter at 280 mm from the source.

For all simulations, the aperture is initially at $z_a$ = 350 mm and increases to 680 mm in steps of $\Delta z_a$ = 1 mm. Taking a 0.1 s exposure time per aperture position, the total equivalent continuous sweep duration would be ~33 s and a sweep velocity of 10 mm $s^{-1}$.

### Annular beam experiments

An annular beam is realized with a geometry as in Fig. 1 and 2 such that $z_D$ = 690 mm, $\phi_{min}$ = 3.87° and $\phi_{max}$ = 3.97°.

In the first set of experiments (i) we replicate the simulation of sucrose ($C_{12}H_{22}O_{11}$) contained in cylindrical plastic containers with sample depth $t$ = 15 mm. The sucrose sample is placed at ~220 ± 10 mm from the X-ray source. A second set of experiments (ii) replicates the simulation of $t$ = 15 mm calcium hydroxide ($Ca(OH)_2$) and $t$ = 15 mm calcite ($CaCO_3$). The powder samples are placed at ~160 ± 10 mm and ~280 ± 10 mm, respectively.

In both sets of experiments, single- and multi-sample, the aperture is initially at $z_a$ = 350 mm and increases to 680 mm in steps of $\Delta z_a$ = 1 mm. The photon collection time at each aperture position is either 0.1 or 0.02 seconds, producing total equivalent sweep durations of ~33 s and 6.6 s respectively, with corresponding aperture sweep velocities of 10 mm $s^{-1}$ or 50 mm $s^{-1}$.

### Spatial sampling

In both simulation and experiment, we sample at regular intervals in $z_a$, collecting photons for a period of 0.1 seconds or 0.02 seconds. This is analogous to a constant aperture sweep velocity of 10 mm $s^{-1}$ or 50 mm $s^{-1}$, respectively. Additionally, there is a non-linear relationship between $z_a$ and $z_C$, leading to a non-linear sampling of $z$-space, weighted towards low $z$. The equivalent continuously swept aperture would be translated at a constant velocity, $\dot{z}_a$ with acceleration $z_a$ = 0. To sample $z$-space at regular intervals would require translation of the aperture with $\dot{z}_a = \dot{z}_a(z_a)$ *i.e.*, non-zero acceleration.

The sampling rate is determined by the aperture translation interval, or the equivalent aperture sweep velocity in a continuously translated system. By increasing either, the aperture translation interval or sweep velocity we can sample $z$-space more sparsely and therefore reduce measurement times. The effect of this sparse sampling is discussed with reference to experiment measurements.

## Results and discussion

### Monte Carlo simulation

A single $t$ = 15 mm region of sucrose ($C_{12}H_{22}O_{11}$) is simulated in the beam path of the annular source described above. Fig. 3 illustrates the energy-resolved intensity measurements at the detector as the aperture sweep enables an increasingly large intersection volume (and solid angle) from which diffracted photons may be detected.

The energy spectrum at each aperture position is integrated (see Fig. 3(b)), revealing a step-like function of aperture position, with a zero-value baseline (instrument noise is not simulated). The rising-edge feature is due to the increasing specimen volume interrogated as afforded by the moving aperture. The response plateau occurs when the maximum specimen thickness remains visible to the detector. A more precise assessment of the sample location requires application of the model in eqn 4(a) and 4(b) to the integrated detector intensity (Fig. 3(b)). The location of sucrose, predicted at the maximum of eqn (5), is calculated as 225 ± 38 mm from the X-ray source. The 'true' spatial range of sucrose in this simulation is 220–235 mm.

In Fig. 4 we reconstruct the diffractogram (with reference standard for comparison) of the object located at 220–235 mm by integration of the detector intensity within each energy bin collected along the plateau region of Fig. 3(b), *i.e.*, $z_C$ > 350 mm.

Next, we simulate the presence of multiple crystalline samples; calcium hydroxide ($Ca(OH)_2$) and calcite ($CaCO_3$), each with $t$ = 15 mm and separated by a centre-to-centre distance of 220 mm along the $z$-axis. The energy-resolved and energy-integrated detector intensities are shown in Fig. 5.

The presence of two crystalline objects in the conical beam path results in a series of step changes in total photon count at the detector and plateau regions. The first plateau, $\tau_1$ includes photons from the object closest to the source (as with the previous single sucrose example) however the second plateau, $\tau_2$ now includes diffracted photons from both the first and second objects. To isolate the second object, we subtract

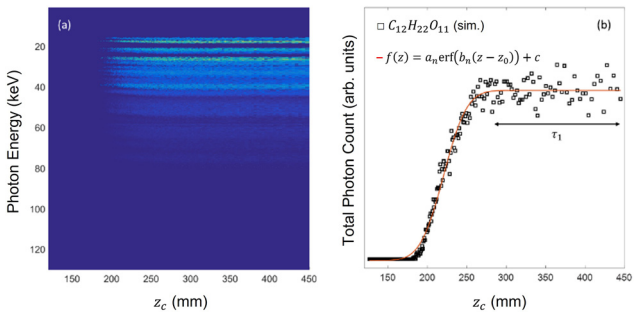


**Fig. 3** Monte Carlo simulation of single $C_{12}H_{22}O_{11}$ sample at 220–235 mm with (a) energy-resolved detector intensity at each maximum observed $z$-axis position. The diffraction lines appear flat because once a 2$\theta$ trajectory has been 'swept through' the resultant signal is invariant to increasing $z_C$ due to the increasing 'solid angle' of scatter capture and (b) energy-integrated detector intensity with single error function model fitted and integration period, $\tau_1$.

 This journal is © The Royal Society of Chemistry 2023

Open Access Article. Published on 16 January 2023. Downloaded on 3/24/2023 9:50:45 AM.
This article is licensed under a Creative Commons Attribution 3.0 Unported Licence.

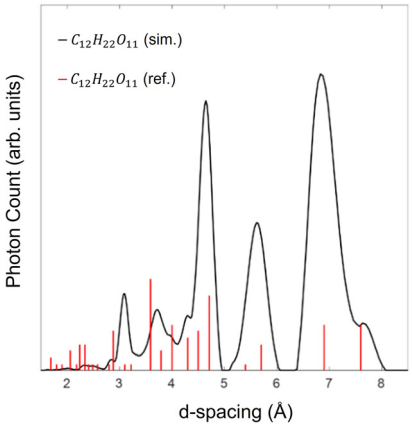


**Fig. 4** Reconstruction of simulated diffractogram of the $C_{12}H_{22}O_{11}$ sample investigated in Fig. 3. Sample location is 225–235 mm from the X-ray source with approximate corresponding diffraction angle, $2\theta$ = 5.8°.

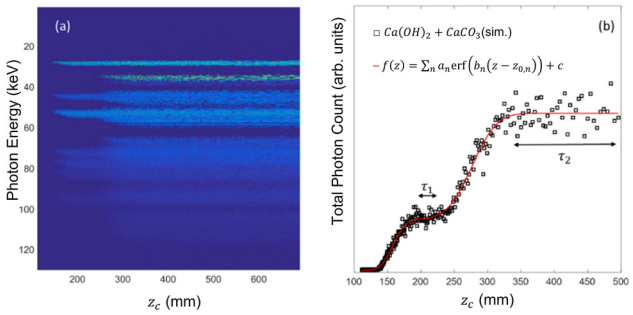


**Fig. 5** Monte Carlo simulation of multiple samples: $Ca(OH)_2$ at 160–175 mm and $CaCO_3$ at 280–295 mm with (a) energy-resolved detector intensity at each maximum observed $z$-axis position and (b) energy-integrated detector intensity with a sum of error functions model fitted and integration periods, $\tau_1$ and $\tau_2$.

the integrated detector signal from the first plateau, weighted to account for sampling frequency within the respective plateaus, from the second.

The first derivative of the LSGI fit now indicates that there are two Gaussian profiles along the $z$-axis centred at 161 ± 26 mm and 282 ± 45 mm. The simulated locations are set at 160–175 mm and 280–295 mm, respectively. Reconstructed diffractogram and reference standards are illustrated in Fig. 6.

### Swept aperture experiments

A single, $t$ = 15 mm sucrose sample is illuminated by the annular source as described. Fig. 7 shows the energy-resolved and energy-integrated detector signal during the translation of the aperture. In contrast to simulation, there is now the presence of a non-zero baseline to the energy-integrated total photon count in Fig. 7(b) arising from system noise. The baseline is compensated by the constant term in the LSGI model $c_{s,0}$.

The first derivative of the LSGI model predicts a sample location $z_{s,n}$ = 229 ± 38 mm or $z_{s,n}$ = 228 ± 38 mm for the $\dot{z}_a$ =

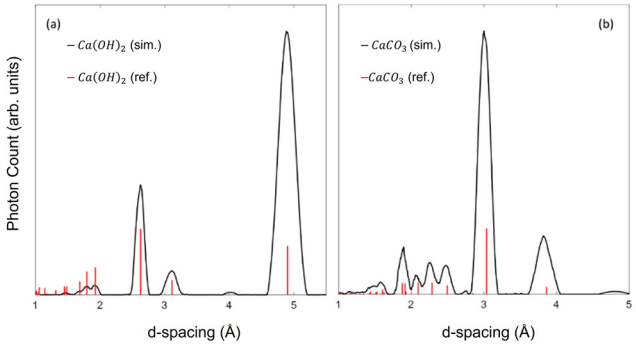


**Fig. 6** Reconstruction of simulated diffractograms of the (a) $Ca(OH)_2$ and (b) $CaCO_3$ samples investigated in Fig. 5. Sample locations are (a) ~161 mm from the X-ray source with approximate corresponding diffraction angle, $2\theta$ = 5.1° and (b) ~282 mm from the X-ray source with approximate corresponding diffraction angle, $2\theta$ = 6.6°.

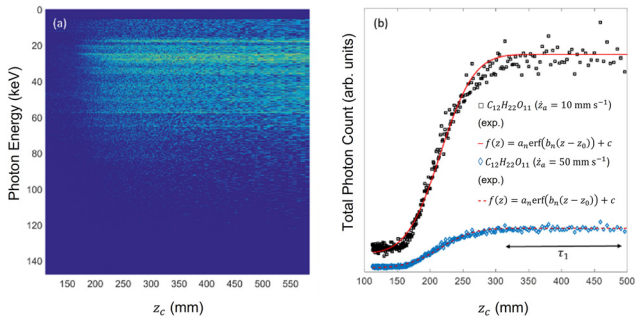


**Fig. 7** Experiment measurement of a single sample at ~220 mm with (a) energy-resolved detector intensity at each maximum observed $z$-axis position; aperture velocity = 10 mm s$^{-1}$ and (b) energy-integrated detector intensity with a single error function model fitted and integration period, $\tau_1$. Measurements recorded at aperture velocities of 10 mm s$^{-1}$ (black squares) and 50 mm s$^{-1}$ (blue diamonds).

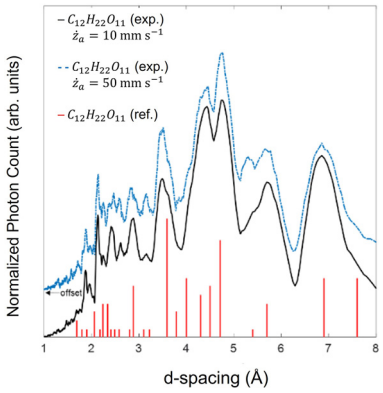


**Fig. 8** Reconstruction of experiment diffractogram of the $C_{12}H_{22}O_{11}$ sample investigated in Fig. 7, with aperture velocities of 10 mm s$^{-1}$ (black, solid) and 50 mm s$^{-1}$ (blue, dashed). Predicted sample location is ~229 mm from the X-ray source.

Open Access Article. Published on 16 January 2023. Downloaded on 3/24/2023 9:50:45 AM.
This article is licensed under a Creative Commons Attribution 3.0 Unported Licence.

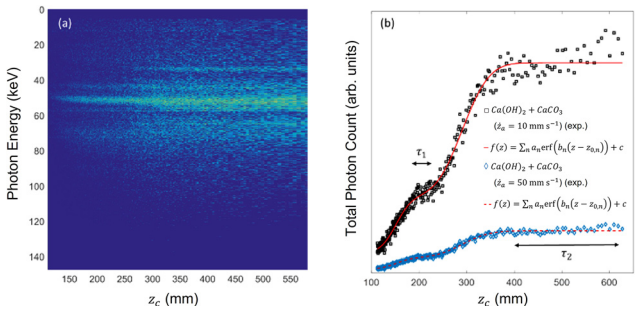


**Fig. 9** Experiment measurement of a multiple samples: $Ca(OH)_2$ at ~160 mm and $CaCO_3$ at ~280 mm with (a) energy-resolved detector intensity at each maximum observed $z$-axis position; aperture velocity = 10 mm $s^{-1}$ and (b) energy-integrated detector intensity with a sum of error functions model fitted and integration periods, $\tau_1$ and $\tau_2$. Measurements recorded at aperture velocities of 10 mm $s^{-1}$ (black squares) and 50 mm $s^{-1}$ (blue diamonds).

10 mm $s^{-1}$ or 50 mm $s^{-1}$, respectively. The corresponding diffractogram reconstruction is illustrated in Fig. 8.

Next, sequential, $t$ = 15 mm regions of $Ca(OH)_2$ and $CaCO_3$ are illuminated by the annular X-ray source. Fig. 9 shows the energy-resolved and energy-integrated detector signal during translation of the aperture.

Two sample responses are indicated in the integrated detector intensity profile. The first derivative of the LSGI model correspondingly predicts two mean sample locations of the 15 mm thick samples; the first sample $Ca(OH)_2$ is likely located at $z_{s,1}$ = 160 ± 25 mm or 159 ± 25 mm for the $\dot{z}_a$ = 10 mm $s^{-1}$ and 50 mm $s^{-1}$ sweeps. The second sample $CaCO_3$ is predicted at $z_{s,n}$ = 302 ± 47 mm or $z_{s,n}$ = 304 ± 47 mm, where the latter (worst case) reconstructed diffractogram is illustrated in Fig. 10.

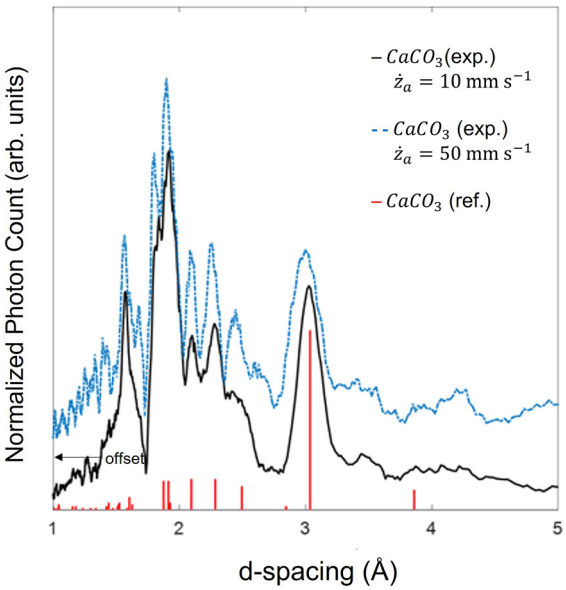


**Fig. 10** Reconstruction of experiment diffractogram of the $CaCO_3$ sample investigated in Fig. 9. Predicted sample location ~ 302 mm with approximate corresponding diffraction angle, $2\theta$ = 6.6°.

## Conclusion

The swept aperture ED-FCT technique can identify multiple object locations along the depth axis and provide material composition information. Measurement times for inspection of an extended $\Delta z$ = 400 mm region of interest are ~40 s and ~8 s, corresponding to X-ray exposures of 12 mAs and 2.4 mAs respectively, depending on the aperture translation speed.

This technique requires collecting spectra from sufficient 'empty' $z$-space before the region of interest. This is because a model fitted to an incomplete step *i.e.*, without a 'baseline plateau' can introduce additional uncertainty in the calculation $2\theta$ for a sample. In practice, this occurrence is accommodated by defining appropriate near and far limits to the inspection region.

In general, most background scatter in a real security luggage screening scenario arises from low density, amorphous materials. As such this scatter has a relatively low magnitude and thus, we fully expect the approach to be applicable even when the volume contains potentially confounding materials. The depth resolution of the probe will certainly help exclude confounding scatter from above and below the target region within the limits of the probe's depth resolution. Where there can be scattering from crystalline 'clutter' then this may be resolved following similar protocols found within the diffractionists' armoury for accommodating mixed phase materials.[37] Also, it is unlikely that any probe technology would circumvent 'dark alarms' as these are due to insufficient X-ray penetration of dense or masked target areas. Thus, for a luggage screening application we recommended a brighter source of around 180 kV, 3 mA in comparison to the one used in our experiments. This would provide increased penetration, in line with current industry practice, and around 20 times the amount of signal photons to improve photon statistics. The depth resolution can be improved by employing a smaller diameter 'point' detector.

For a security application that only requires a phase identification, no refinement of the data is required although conventional match indices could be applied. For more detailed analysis beyond simple phase, the data could be refined against a structural model,[38] but the unique geometry would result in specific and non-conventional parameter forms of, for example, Lorentz and absorption corrections.

The compact probe architecture uses cost-effective point detector technology and is scalable in both X-ray energy and inspection space. Potential applications include false alarm resolution in security luggage screening, process control and medical diagnostics.

## Conflicts of interest

There are no conflicts of interest to declare.

 This journal is © The Royal Society of Chemistry 2023

Open Access Article. Published on 16 January 2023. Downloaded on 3/24/2023 9:50:45 AM.
This article is licensed under a Creative Commons Attribution 3.0 Unported Licence.

## Acknowledgements

This work was funded by The Royal Society and The Wolfson Foundation RSWF\R1\180012; The Department of Homeland Security (DHS), Science and Technology Directorate, Homeland Security Advanced Research Projects Agency, Explosives Division through the Advanced X-ray Material Discrimination Program (HSHQDC-15-CB0036); and the Engineering and Physical Sciences Research Council EP/T034238/1.

## References

1 S. Singh and M. Singh, *Signal Process.*, 2003, **83**(1), 31–55.
2 G. Harding and A. Harding, 8 - X-ray Diffraction Imaging for Explosives Detection, in *Counterterrorist Detection Techniques of Explosives*, ed. J. Yinon, Elsevier Netherlands, 1st edn, 2007, pp. 199–235.
3 J. A. Greenberg and J. Carpenter, 9 - X-ray diffraction for explosives detection, in *Counterterrorist Detection Techniques of Explosives*, ed. A. Kagan and J. C. Oxley, Elsevier Science, 2nd edn, 2022, pp. 315–338.
4 S. R. Purohit, L. E. Jayachandran, A. S. Raj, D. Nayak and P. S. Rao, 22 - X-ray diffraction for food quality evaluation, in *Evaluation Technologies for Food Quality*, ed. J. Zhong and X. Wang, Elsevier Woodhead, 2019, 579–594.
5 B. B. He, 11-Combinatorial Screening, in *Two-Dimensional X-Ray Diffraction*, Wiley, USA, 2009, pp. 351–368.
6 A. J. Dicken, J. P. O. Evans, K. D. Rogers, N. Stone, C. Greenwood, S. X. Godber, D. Prokopiou, J. G. Clement, D. Lyburn, R. M. Martin and P. Zioupos, *Phys. Med. Biol.*, 2015, **60**, 5803–5812.
7 C. Greenwood, K. Rogers, M. Wilson, I. Lyburn, P. Evans and D. Prokopiou, Developing focal construct technology for in vivo diagnosis of osteoporosis, *J. Phys.: Conf. Ser.*, 2019, **1151**, 012020, IOP Publishing.
8 A. J. Dicken, J. P. O. Evans, K. D. Rogers, N. Stone, C. Greenwood, S. X. Godber, J. G. Clement, I. D. Lyburn, R. M. Martin and P. Zioupos, *Sci. Rep.*, 2016, **6**, 29011.
9 A. R. Round, S. J. Wilkinson, C. J. Hall, K. D. Rogers, O. Glatter, T. Wess and I. O. Ellis, *Phys. Med. Biol.*, 2005, **50**, 4159–4168.
10 W. C. Rontgen, *Nature*, 1896, **53**(1369), 274–277.
11 W. Bragg, *Nature*, 1912, **90**, 410.
12 I. Drakos, P. Kenny, T. Fearn and R. Speller, *Crime Sci.*, 2017, **6**(1), 1.
13 J. A. Greenberg, M. Hassan, K. Krishnamurthy and D. Brady, *Analyst*, 2014, **139**, 709–713.
14 D. O'Flynn, C. Crews, I. Drakos, C. Christodoulou, M. D. Wilson, M. C. Veale and R. Speller, *J. Phys. D: Appl. Phys.*, 2016, **49**(17), 175304.
15 S. F. Nielsen, E. M. Lauridsen, D. J. Jensen and H. F. Poulsen, *J. Mater. Sci. Eng. A*, 2001, **319–321**, 179–181.
16 R. J. Cernik, K. H. Khor and C. Hansson, *J. R. Soc., Interface*, 2008, **5**(21), 477–481.
17 O. Lazzari, S. Jacques, T. Sochi and P. Barnes, *Analyst*, 2009, **134**, 1802–1807.
18 K. Wells and D. A. Bradley, *Appl. Radiat. Isot.*, 2012, **70**(8), 1729–1746.
19 A. Vamvakeros, S. D. M. Jacques, M. Di Michiel, P. Senecal, V. Middelkoop, R. J. Cernik and A. M. Beale, *J. Appl. Crystallogr.*, 2016, **49**, 485–496.
20 R. Warr, E. Ametova, R. J. Cernik, G. Fardell, S. Handschuh, J. S. Jørgensen, E. Papoutsellis, E. Pasca and P. J. Withers, *Sci. Rep.*, 2021, **11**, 20818.
21 C. K. Egan, S. D. M. Jacques, M. D. Wilson, M. C. Veale, P. Seller, A. M. Beale, R. A. D. Pattrick, P. J. Withers and R. J. Cernik, *Sci. Rep.*, 2015, **5**, 15979.
22 G. Artioli, T. Cerulli, G. Cruciani, M. C. Dalconi, G. Ferrari, M. Parisatto, A. Rack and R. Tucoulou, *Anal. Bioanal. Chem.*, 2010, **397**, 2131–2136.
23 E. Possenti, C. Conti, G. D. Gatta, N. Marinoni, M. Merlini, M. Realini, G. B. M. Vaughan and C. Colombo, *iScience*, 2022, **25**(10), 105112.
24 P. Evans, K. Rogers, J. Chan, J. Rogers and A. Dicken, *Appl. Phys. Lett.*, 2010, **97**, 204101.
25 K. Rogers, P. Evans, J. Rogers, J. Chan and A. Dicken, *J. Appl. Crystallogr.*, 2010, **43**(2), 264–268.
26 K. Rogers and P. Evans, X-ray diffraction and focal construct technology, in *X-Ray Diffraction Imaging: Technology and Applications*, ed. J. Greenberg, Taylor and Francis Group, 2019, 165–188.
27 A. Dicken, J. P. O. Evans, K. D. Rogers, C. Greenwood, S. X. Godber, D. Prokopiou, N. Stone, J. G. Clement, I. Lyburn, R. M. Martin and P. Zioupos, *Opt. Express*, 2015, **23**(10), 13443–13454.
28 D. Prokopiou, K. Rogers, P. Evans, S. Godber and A. Dicken, *Appl. Radiat. Isot.*, 2013, **77**, 160–165.
29 F. Li, Z. Liu, T. Sun, B. Jiang and Y. Zhu, *J. Chem. Phys.*, 2016, **144**, 104201.
30 X. H. Chen, B. Li, T. Xue and J. Li, *Rev. Sci. Instrum.*, 2020, **91**, 083908.
31 D. Prokopiou, J. McGovern, G. Davies, S. Godber, P. Evans, A. Dicken and K. Rogers, *J. Appl. Crystallogr.*, 2020, **53**(4), 1073–1079.
32 A. Dicken, A. Shevchuk, K. Rogers, S. Godber and P. Evans, *Opt. Express*, 2015, **23**(5), 6304–6312.
33 P. Evans, K. Rogers, A. Dicken, S. Godber and D. Prokopiou, *Opt. Express*, 2014, **22**(10), 11930–11944.
34 A. Dicken, J. P. O. Evans, K. D. Rogers, D. Prokopiou, S. X. Godber and M. Wilson, *Opt. Express*, 2017, **25**(18), 21321–21328.
35 A. Dicken, D. Spence, K. Rogers, D. Prokopiou and P. Evans, *Analyst*, 2018, **143**(20), 4849–4853.
36 E. B. Knudsen, A. Prodi, J. Baltser, M. Thomsen, P. K. Willendrup, M. Sanchez del Rio, C. Ferrero, E. Farhi, K. Haldrup, A. Vickery, R. Feidenhans'l, K. Mortensen, M. M. Nielsen, H. F. Poulsen, S. Schmidt and K. Lefmann, *J. Appl. Crystallogr.*, 2013, **46**(3), 679–696.
37 R. F. Karlak and D. S. Burnett, *Anal. Chem.*, 1966, **38**(12), 1741–1745.
38 L. B. McCusker, R. B. Von Dreele, D. E. Cox, D. Louër and P. Scardi, *J. Appl. Crystallogr.*, 1999, **32**(1), 36–50.

**Cranfield University**

**CERES Research Repository** **https://dspace.lib.cranfield.ac.uk/**

Cranfield Defence and Security Staff publications (CDS)

# Conical shell illumination incorporating a moving aperture for depth-resolved high-energy X-ray diffraction

Spence, Daniel

2023-01-16

Attribution 4.0 International

Spence D, Dicken A, Downes D, et al., (2023) Conical shell illumination incorporating a moving aperture for depth-resolved high-energy X-ray diffraction, The Analyst, Volume 148, Issue 5, 7 March 2023, pp. 1123-1129

https://doi.org/10.1039/D2AN01842J

*Downloaded from CERES Research Repository, Cranfield University*